JGR Space Physics

RESEARCH ARTICLE
10.1029/2020JA028299

Inflow Speed Analysis of Interchange Injections in Saturn's Magnetosphere

C. Paranicas[1], M. F. Thomsen[2], P. Kollmann[1], A. R. Azari[3], A. Bader[4], S. V. Badman[4], M. Dumont[5], J. Kinrade[4], N. Krupp[6], and E. Roussos[6]

[1]APL, Laurel, MD, USA, [2]Planetary Science Institute, Tucson, AZ, USA, [3]Space Sciences Laboratory, University of California, Berkeley, CA, USA, [4]Department of Physics, Lancaster University, Lancaster, UK, [5]STAR Institute, LPAP, University of Liège, Liège, Belgium, [6]Max Planck Institute for Solar System Research, Goettingen, Germany

Key Points:
- We describe a new method to characterize inflow speeds of interchange injections at Saturn
- We estimate average radial inflow speeds of 22 km/s
- We provide a table of mappings and find interchange injections typically travel one to two Saturn radii

Correspondence to:
C. Paranicas,
chris.paranicas@jhuapl.edu

Citation:
Paranicas, C., Thomsen, M. F., Kollmann, P., Azari, A. R., Bader, A., Badman, S. V., et al. (2020). Inflow speed analysis of interchange injections in Saturn's magnetosphere. *Journal of Geophysical Research: Space Physics*, *125*, e2020JA028299. https://doi.org/10.1029/2020JA028299

Received 2 JUN 2020
Accepted 1 SEP 2020
Accepted article online 4 SEP 2020

Abstract During its more than 13 years in orbit, the Cassini spacecraft detected a large number of plasma and energetic charged particle injections in Saturn's inner magnetosphere. In the corotating frame of the planet, the plasma contained within an injection moves radially inward with the component particles gaining energy. The highest energy particles in the injection experience stronger gradient-curvature drifts in the longitudinal direction and can drift out of the main body of the injection. We have used these drift-out effects to estimate the inflow speed of 19 injections by surveying cases from the available plasma data. We find that the average inflow speed from our sample is 22 km/s, and the values are well distributed between 0 and 50 km/s, with a few higher estimates. We have also computed the radial travel distance of interchange events and found that these are typically one to two Saturn radii. We discuss the implications of these quantifications on our understanding of transport.

1. Introduction

Due to the large population of neutrals in Saturn's inner magnetosphere, hot plasma does not survive indefinitely. While the corotating plasma can coexist with the gas, hotter ions can undergo loss processes including charge exchange, where they exit the magnetosphere as neutrals, carrying away their energy. Other plasma components like hot plasma electrons can lose energy in multiple collisions with the ambient particles and through wave-particle interactions. Consequently, the flux of the quasi-stably trapped hot plasma can be very low in the inner magnetosphere of Saturn, making it easy to identify new injections into this region of the magnetosphere and their detailed features.

Earlier papers that focused on the radial motion of injections in Saturn's magnetosphere (e.g., Burch et al., 2005; Hill et al., 2005; Paranicas et al., 2016; Rymer et al., 2009) did so with the goal of making our knowledge of the recirculation process more quantitative. It is believed that the new plasma continuously supplied in connection with the Enceladus plumes must be shed outward. Hotter plasma moves inward toward the planet through the conservation of magnetic flux. This scenario has been modeled in two dimensions using the Rice Convection Model (e.g., Liu et al., 2010). Those simulations illustrate longitudinally narrow fingers of hot inflowing plasma interspersed with longitudinally extended distributions of cold plasma moving outward.

Wilson et al. (2008, 2017) and Chen et al. (2010) characterized the radial motion of Saturn's plasma, excluding intervals of interchange. In addition, a comprehensive review of injections in Saturn's magnetosphere has been carried out by Thomsen (2013) and we will not repeat that material here. More specifically relevant to this paper is our earlier analysis (Paranicas et al., 2016). There we developed a technique of estimating the radial inflow speed of injections that was based on similar techniques of phase space density (PSD) mapping and a test particle simulation of the drift out process for higher energy plasma. Drift out in this paper will specifically mean the escape of higher energy particles from the main injection due to gradient-curvature drifts in the longitudinal direction. In our earlier work, we analyzed three separate events in detail and found inflow speeds in the range 9–18 km/s.

Since Paranicas et al. (2016) used a very limited sample size, it provided only a snapshot of the possible range of inflow speeds. Estimating an accurate inflow speed is of critical importance to future Saturn studies. From Cassini, it is now known that interchange injections are a major mass transport system (e.g.,

Thomsen, 2013). There are many unanswered questions about this system, which can be informed by improving these velocity estimations. For example, do some injections show a marked enhancement in velocity above others? If so, what is the origin of this acceleration? Such patterns would imply temporal variations in the dynamics of Saturn's magnetosphere that go beyond the "quasi-steady" (Thomsen, 2013) scenarios that models have produced.

Estimations of inflow velocities have been extremely challenging to produce. At first pass, the instruments onboard Cassini often do not return a fast enough cadence to characterize the highly dynamic nature of interchange. Events are often observed lasting for 15 min or less (Azari et al., 2018). Gathering accurate inflow speeds has been a large focus of interchange studies.

In this paper, we have extended that earlier work with the Cassini Plasma Spectrometer (CAPS) data (see Young et al., 2004) with events selected from the entire period of Cassini orbit when CAPS was operating. We chose a subset of events where the drift out feature is very clear. We again use PSD mapping techniques. However, we now consider that quantity for multiple energies, to provide a more complete picture of the injection starting location, consistent across energy ranges. The other major change implemented in this study is that we no longer fit the shape of the energetic particles that have not escaped the injection using our test particle model. Instead, we approximate the drift out times using another approach described below.

2. Drift Out Process

The plasma moves under the influence of the background magnetic field (B) and the corotation electric field (E). The main perturbation is the dE × B drift associated with the injection, where dE points in the longitudinal direction. Cassini data from interchange events show the magnetic perturbation is no more than a few nanotesla (e.g., Andre et al., 2005), so the inwardly moving distribution is essentially guided by the background fields plus the radial dE × B.

The guiding center motion of charged particles within a magnetosphere is commonly represented as the sum of an E × B drift, which is the same for all particles independent of energy or species, and a gradient-curvature drift that depends on energy and species (e.g., Walt, 1994). At Saturn, the E × B drift dominates the motion of particles at low energies. For example, the gradient-curvature drift speed divided by the corotation speed is about 0.01 at L = 5 for a nearly equatorial, 1 keV electron. At higher energies, the gradient-curvature drifts due to the magnetic field (Walt, 1994) begin to cause a more meaningful separation of the hotter plasma from the colder plasma. In the corotating frame of the plasma, more energetic electrons within an injection drift westward and can exit the injection channel through the edge. Once they are located well away from the channel, they are no longer subject to the dE × B and remain on the same L shell. Andre's work (Andre et al., 2005, 2007) has shown that the dB associated with interchange is not uniform along the field line and changes sign at a few degrees off the magnetic equator. Therefore, gradients in B near the edges of the distribution will likely only slightly alter the trajectory of the drift out, adding a small dr toward the planet at low latitudes and a small outward drift at higher latitudes. These facts also suggest to us that drift out is not typically impeded, for example, by gradients in B near the injection edges.

During the drift out process, it is easy to see that the flux of the higher-energy electrons just inside the eastern edge of the injection goes to zero. That region is depleted by the westward drift of the hot electrons within the injection. When the trailing side of the injection reaches the spacecraft, the electrons fall off steeply near the edge; see also Burch et al. (2005).

In Figure 1, we show an electron injection detected by Cassini/ELS on day 2011-010 at about 21:08 UT. In this view, the right-hand side (RHS) has a vertical edge such that all energies experience a significant change in flux at approximately the same time. (This is the western edge of the population.) The small amount of energy dispersion at the trailing edge likely suggests that the injection channel has not been present at this L value for long enough for a significant number of higher-energy electrons to escape locally from the flux tube. The leading/eastern edge (left-hand side, LHS), on the other hand, shows the drift-out depletion feature, which reveals the accumulated loss of particles during the inward propagation of the channel. During the inward flow, the higher energies have drifted out faster, so the extent of the drift-out is greater with increasing energy. Although the flux within this particular event is not monotonic, it is still possible to see a progression in flux with energy along the LHS edge, for example, see the line plots.

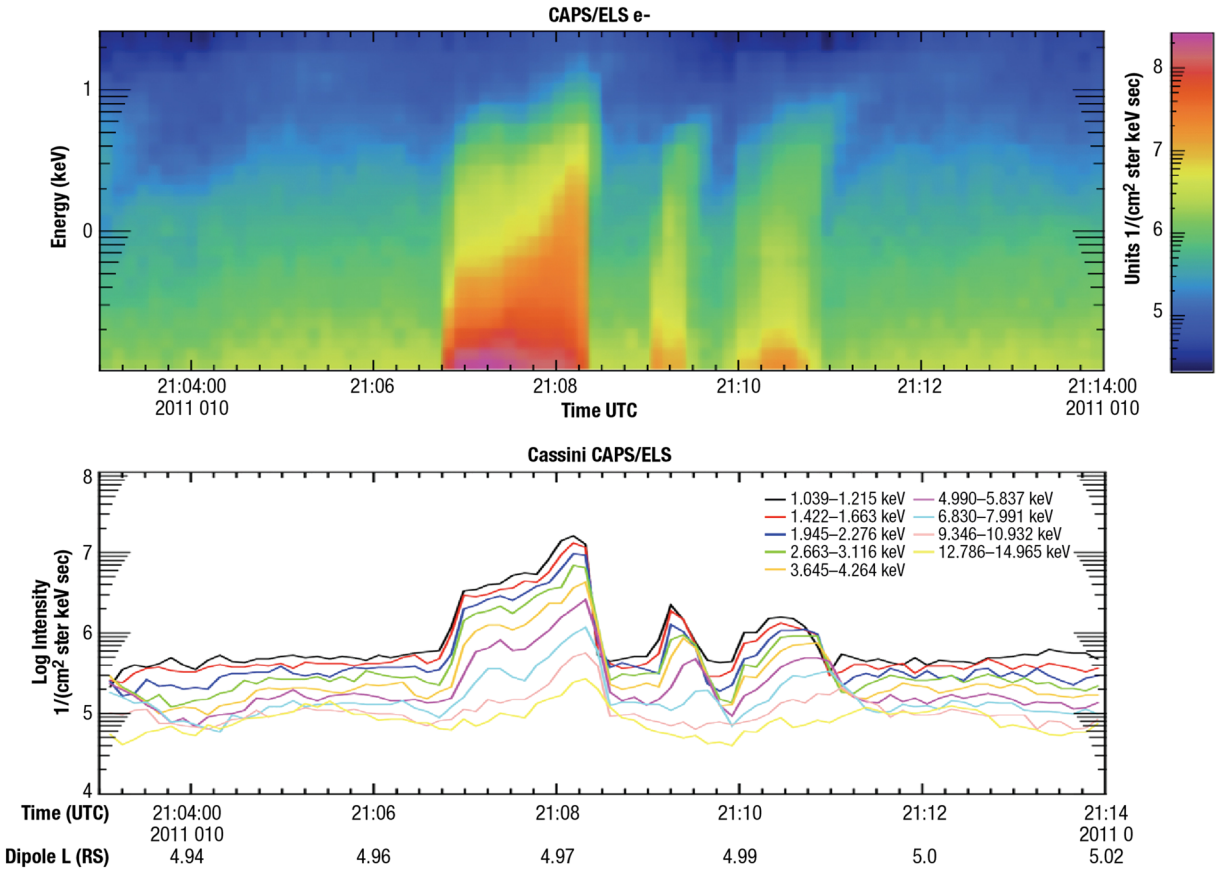

Figure 1. CAPS/ELS electron data from day 2011-010 21:03 to 21:14 UT. The top panel shows intensity versus time and log10 (energy in keV). A horizontal line at 2 keV through the main structure shows how the flux increases at that energy toward the trailing edge. The lower panel shows individual energies as line plots very intensity.

In Figure 2, we show what we believe to be a much more rapid inflow event at larger L shells on day 2005-068 at 00:49 UT. This could be a double structure since the line plots do not show a constant flux inside the structure but instead a dip in flux around 00:51. The LHS shows the depletion pattern of drift out consistent with other events. The electrons relatively unaffected by drift-out, that is, those below about 1 keV, show a change in flux at about 00:49:30 UT, at what we are calling *the edge*. The increase in flux to a nearly constant level occurs at about 00:49:45 for 1 keV electrons and at 00:50:30 for electrons at 3.5 keV or so. These are approximately 15 and 60 s from the edge and, hence, these time separations from the edge scale in the same way as energy. This underlines the fact that the drift out concept is reasonably consistent with numerical expectations.

3. Procedure

To quantify the radial inflow speed of injections, we must find the starting L shell (Ls) of each event. As in previous studies (Burch et al., 2005; Paranicas et al., 2016), we make the assumption that PSD is conserved at constant first adiabatic invariant, μ. We ignore the second adiabatic invariant, J, which typically changes the equatorial pitch angle by a small amount over the radial range we are considering here (e.g., Figure 5 of Paranicas, Mitchell, Krimigis, et al., 2010). Then we map the observed PSD, f, at a given value of the first invariant to the region where the ambient PSD at that value of the first invariant has the same value of f, which determines Ls (e.g., Paranicas et al., 2016). We use a smoothed version of the recent PSD profile. Complete details of how this is done are provided in the Appendix.

The exact edges of the injection are determined by the lowest energies of the injection (i.e., those least subject to the magnetic gradient and curvature drifts). The color plot in Figure 1 shows two clear examples of

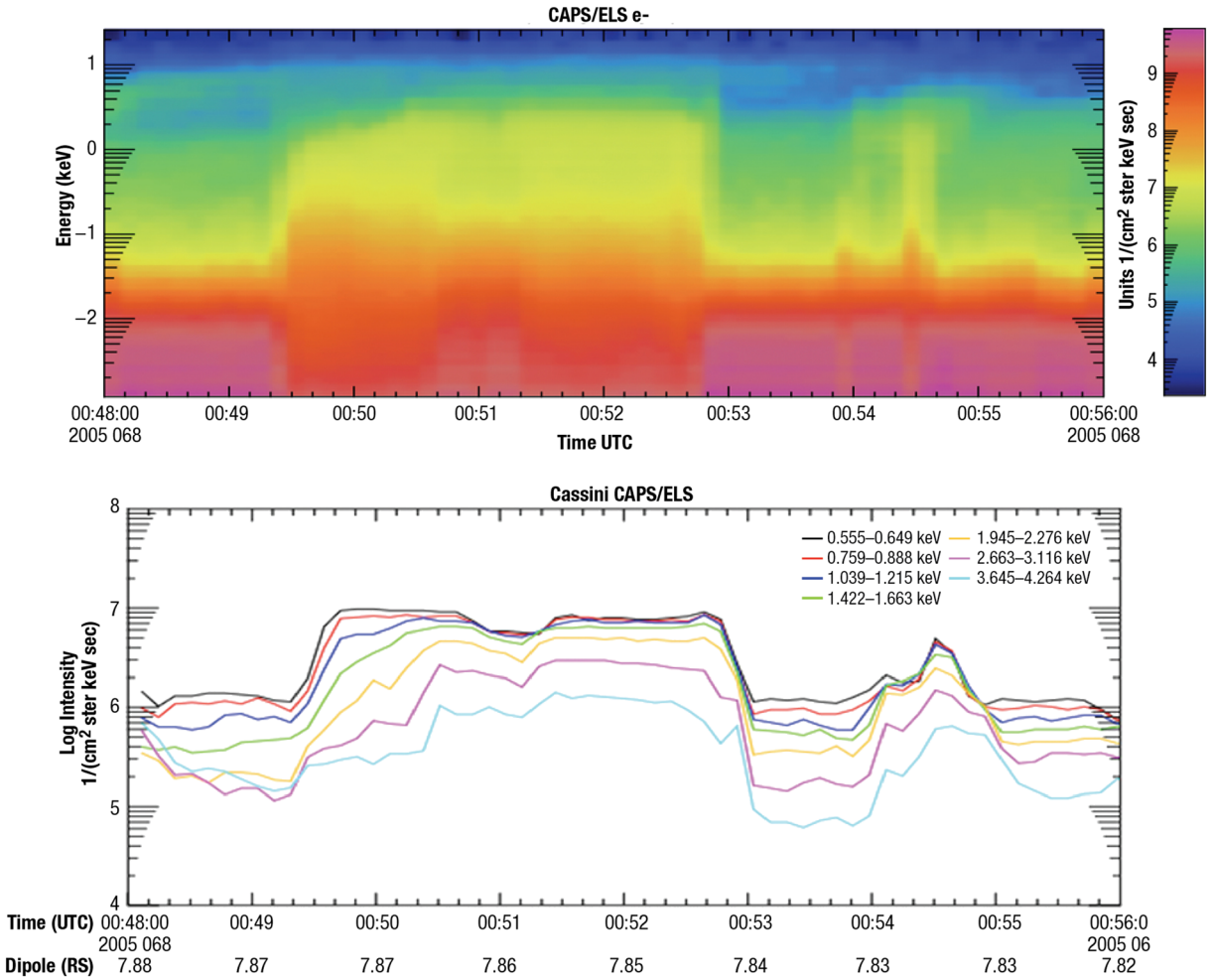

Figure 2. Similar display as in Figure 1 for day 2005-068 00:48 to 00:56 UT.

injection edges at 100 eV. Then the gap between the eastern wall of the injection and the first populated longitude at any given energy, E, can be estimated as follows. As the particles drift radially inward across an L shell by an amount dL, the longitudinal separation between the hot plasma and the injection edge increases by the amount, ~ω × dt × R_S × L, where ω is the gradient-curvature drift in the subcorotating frame at the current L and E, assuming the particles are all nearly equatorially mirroring (Thomsen & Van Allen, 1980), R_S is the radius of Saturn, and dt is the time the injected particles traveled across dL. We assume the plasma is subcorotating at each L using the estimate provided in Mauk et al. (2005). The energy at each timestep is determined assuming μ is conserved in a dipole field. Then we add up these longitudinal drift increments over the radial path of the particle to form a total d, the distance in km at the observation L shell between the edge of the injection and the hot plasma of energy E inside the injection. We assume a constant inflow speed in our work. This is justified by the small distances over which these injections travel, as we discuss below. In Figure 3, we show, for illustrative purposes only, an example of the quantity d as a function of inflow speeds. Here we assumed electrons mirroring close to the magnetic equator moved from Ls = 7 to Le = 5 and had a final energy of 3 keV. Each event we analyze will have a unique d curve. For comparison to an actual event, the ~14 keV electrons in Figure 2 would have d = 3,324 km for an inflow speed of 35.5 km/s.

When the gap between the injection edge and the hot plasma inside the injection, d, is compared to data, we can constrain the inflow speed. Based on this discussion, for the event in Figure 1, the range of starting locations was determined to be Ls = 6.32 to Ls = 7.63, from which we estimate the inflow speed to the ending or detection L shell, Le = 4.97, as between 4.1 and 14.5 km/s. For the event depicted in Figure 2, we believe the

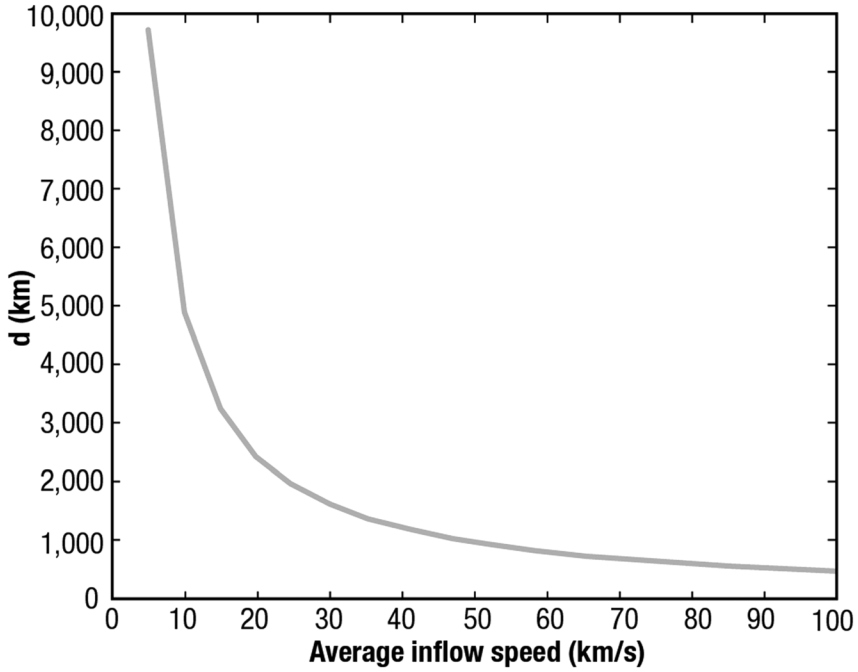

Figure 3. Model separation (d in km) between the remaining trapped flux and an injection edge in the longitudinal direction. The injected electrons traveled from L = 7 to L = 5 at various constant inflow speeds (x axis) and had final energy 3 keV.

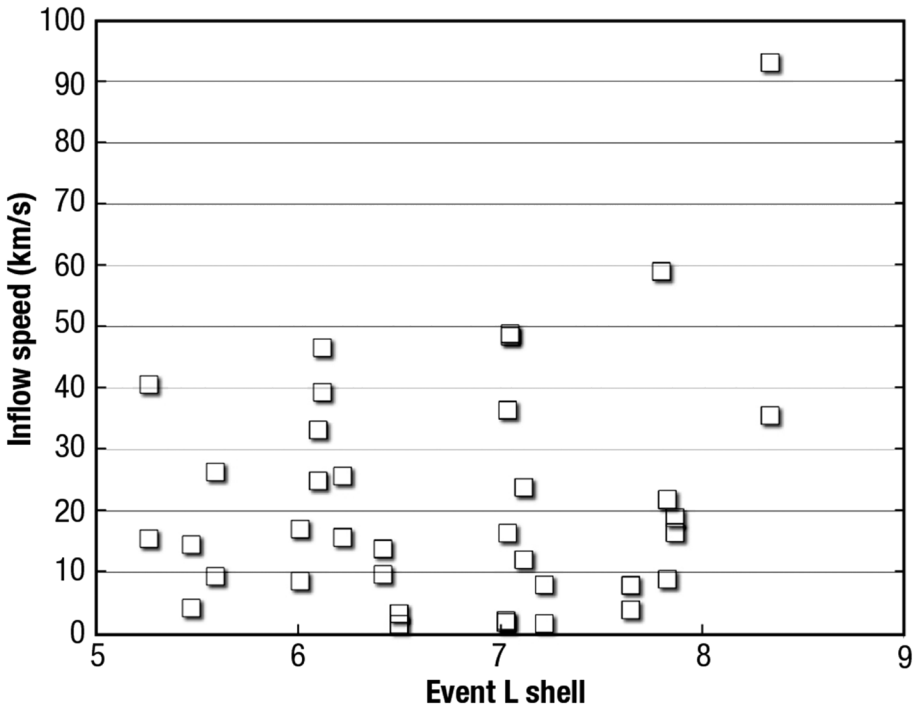

Figure 4. Inflow speed (in km/s) summary plotted at Le for all 19 events. In all but one case, the two inflow speeds selected at each L corresponded to averaging the possible starting distances found and then using ±1 standard deviation from the average. Two sets of events near L = 7 have very small radial spreads.

Ls range is 8.86 to 9.88, so that with Le = 7.84, the inferred radial inflow speed range is ~36–93 km/s. Recall the amount of drift out (i.e., the gap) is a factor in the speed determinations.

In Figure 4, we show a summary of the inferred inflow speeds of the 19 events we have considered at the location the events were detected. Almost all the events had a range of possible starting L shells, determined by mapping the PSD at different energies associated with the injection, and we chose two values of Ls to analyze. For the pair of points plotted at Le = 4.97 (from an injection at 2011–0102108 UT; see Figure 1 and Table A1), for example, we used Ls values of 6.32 and 7.63. For the pair of points at Le = 5.72 (from 2005-359 0250 UT), we used 6.68 and 7.06 and the inflow speed estimate varied by less than a factor of 2. We did not consider some events in the figure (e.g., day 2010-206 10:20), because Ls was not clear. A starting L greater than a fixed value is not precise enough for this kind of analysis and because of the possibly long travel distance, would give a very high inflow speed. As the plot shows, most of the inferred inflow speed estimates are below about 50 km/s.

4. Summary and Conclusions

We have surveyed the CAPS data set from Cassini's Saturn tour to identify injections that reveal the effects of electron drift out at the highest energies of the injection. Choosing the most straightforward examples, we use the separation between the eastern/leading edge of the injection (determined by colder plasma) and the population strongly affected by drift out to estimate a time that had elapsed from the injection start location to the measurement location. Overall, our analysis indicates that the various energies show a sensible ordering in the size of the longitudinal gap between the trapped flux and the eastern edge consistent with a drift out picture. By combining this with PSD mapping from Ls to Le, we have estimated the inflow speed range.

As in our earlier work, we find inflow speeds in the tens of km/s. For this work, most of the injections were analyzed for drift out features below 20 keV. It is possible that for injections that are very large spatially (e.g., have more significant longitudinal extents), the effect could extend to much higher energies. We have also found that this group of interchange injections have starting locations inward of the plasmapause boundary (Thomsen & Coates, 2019). In addition, our analysis suggests these interchange injections have moved only one or two Saturn radii inward before detection.

Many of the inflow speeds we report on here are larger than the radial flow speeds of the plasma generally expected at Saturn (e.g., Chen et al., 2010; Wilson et al., 2008). Those speeds can alternatively be thought of as a transient, nearly noon-to-midnight electric field, documented by several authors of this paper and others. The relationship between the speed of a small plasma parcel or a flow channel, whichever way the injection is characterized, and Saturn's main plasma may be a complex one. The radial flow speeds in the first case are organized by local time whereas the speeds we extract from the data here are fixed in the corotating frame.

The importance of the inflow speeds reported on here is not directly linked to the planetary (transient) electric field. Instead they are important for understanding several aspects of the transport. The inflow speeds and starting L shells give us a way to quantify what particle species, energies, and charge states can be entrained within injections (without drifting out first). For instance, higher charge state ions have slower gradient-curvature drift and may be able to reach deeper into the magnetosphere than the same ions of equal energy but lower charge state. There are very few predictions of injection inflow speed in the literature, and this work will add importantly to our knowledge of the subject.

Another critical development here is the mapping of injections to their starting locations. It has been assumed that some injections are remnants of larger-scale processes, so that large radial ranges would not be surprising between the starting and detected L shell. The relatively short distances that injections travel possibly suggests another picture, one in which an unstable plasma has interchanges closer to the theoretical picture, one flux tube exchanging for its neighbor. If we were to interpret these short distances in a flow channel picture, then we would have to conclude the reservoir of plasma they start from has a boundary that moves in and out and is not fixed in a particular region.

Appendix A: Determination of Initial Injection Location

From the shape of the drift-out signature at higher energies, it is possible to estimate the time between initial injection and the observation of the injection event at Cassini. In order to use that to estimate the inflow

velocity of the injected particles, it is necessary to know the radial distance at which the injected population originated. For the conceptual model they used to illustrate the drift-out explanation of the injection profile, Burch et al. (2005) assumed the injection initially originated at L = 10, which, with an inflow speed of 25 km/s, reproduced the observed shape of the energy-time spectrum reasonably well. Rymer et al. (2009) estimated the injection origin by locating the radial distance at which the electron PSD matched the value observed within the injection. They assumed that during the transport, the PSD at constant μ and J is conserved. For a single value of (μ, J), they found that six injection events observed on three different days (at L ~ 7.0, 8.1–8.3, and 7.3–7.7) apparently originated beyond 7.8, 9.1, and 8.5 R_S, respectively. We similarly used PSD mapping (Paranicas et al., 2016) to identify the injection's starting distance from Saturn, again assuming conservation of μ and J, with the main difference that the background PSD profile was taken to be the mission-averaged profile, rather than the profile from the current pass. For the three events we analyzed, the derived starting locations were L ~ 7.2, 8.6, and 9.0 for injections observed at L ~ 5.9, 7.2, and 7.2, respectively.

In order to provide starting locations for the events modeled in this paper, a more comprehensive PSD-mapping analysis has been conducted. Starting with a list of injection events compiled by the International Space Science Institute team on "Modes of Radial Transport in Magnetospheres," PSD profiles were produced for several different μ values for each of 32 individual injections, resulting in 173 independent PSD mappings.

Under the assumption of the conservation of μ and J, the PSD profile for any given value of (μ, J) would be based on an interpolation of the observed flux distribution in energy and pitch angle (E, α) to the values of E and α that correspond to the chosen values of μ and J at each measurement point. In practice, we have found that the pitch angle dependence at the energies of interest here is relatively weak, suggesting some amount of pitch angle scattering occurs as charged particles are transported into the inner magnetosphere. Accordingly, we simply assume that the local omnidirectional average (i.e., average over the 8 ELS anodes) appropriately characterizes the flux of equatorially mirroring particles at any given energy, and we use it to estimate the PSD of particles of a specified μ and a nominal equatorial pitch angle of 90°. Under this assumption and the reasonable assumption that the magnetic field is nearly dipolar, the energy at a constant μ scales as $E(\mu, L) \sim L^{-3}$. Alternatively, Rymer et al. (2007) assumed that electrons within the inner magnetosphere undergo strong, but elastic, pitch angle scattering such that they isotropize at essentially constant energy. Under those conditions, electrons approximately conserve a so-called "isotropic invariant," which was previously described by Schulz (1998), and for which the particle energy scales as $E(L) \sim L^{-8/3}$. As illustrated in Figure 4 of Rymer et al. (2007), the L dependence of the electron energy is quite similar for these two approaches, so our results would likely be very similar if we based the profiles on the isotropic invariant. Hence, the PSD profiles here have been computed by interpolating the local omnidirectional averaged flux to $E(L) = E_o * (L_o/L)^3$, where E_o is the energy of the particles of interest at L_o.

Figure A1 shows an example of the derived PSD profile for particles with μ = 3,086 keV/G and J ~ 0 for an inbound pass through the inner magnetosphere on day 2010–205 (blue curve). The time resolution of the measurements is 2 s. The injection of interest occurred at ~2015 UT, at L ~ 6.0. It is marked with the vertical red dashed line. The gold curve in Figure A1 shows the mission-averaged value of PSD at this value of μ, and the red curve shows a 200-point smoothing of the blue PSD profile from the current pass. The smoothed curve eliminates much of the high-frequency variation that makes it difficult to reproducibly identify where the injection PSD intersects the recent data. The smoothing window of 200 points is chosen because it represents approximately a full actuation cycle for the CAPS instrument (Young et al., 2004) and, thus, encompasses the full range of available pitch angles for the omnidirectional average. To map the injection, the peak PSD in the 2-s curve is projected in L to the location where it first intersects the smoothed local pass (vertical blue dashed line). The inferred origin distance is thus ~6.57. For this pass, the smoothed profile from the current pass yields a considerably different mapping distance than would be obtained from the mission-averaged profile, although for many of the events they are quite similar.

The process illustrated in Figure A1 has been repeated for the 173 PSD profiles derived for the 32 identified injections. Table A1 and Figure A2 summarize the results: For each injection, the figure shows the average of the mapped L values for all of the μ values for which a mapping could be determined, and the bars show the resulting standard deviations. The mapped L values, representing the inferred origin distance, are plotted as

Table A1

Table of Mapped Injection Events With Time of Event, L (Event) Is the L Shell Cassini Detected the Event, a Representative Energy of the Injection Computed at Lo, Corresponding First Adiabatic Invariant, and L (Map) Is the Inferred Starting Location Using That Energy and a Set of PSD Profiles

Year	Day	Hour	Minute	L (event)	E(L_0) (keV)	L_0	μ (keV/G)	L (map)
2005	48	7	1	5.51	0.1	6.68	1.419E+02	5.96
2005	48	7	1	5.51	0.3	6.68	4.258E+02	5.96
2005	48	9	25	6.70	1	6.68	1.419E+03	7.86
2005	48	9	25	6.70	3	6.68	4.258E+03	8.00
2005	48	9	25	6.70	6	6.68	8.517E+03	8.01
2005	48	9	25	6.70	10	6.68	1.419E+04	8.31
2005	48	9	48	7.00	1	6.68	1.419E+03	8.27
2005	48	9	48	7.00	3	6.68	4.258E+03	8.29
2005	48	9	48	7.00	6	6.68	8.517E+03	8.01
2005	48	9	48	7.00	10	6.68	1.419E+04	7.90
2005	67	20	18	10.02	0.6	7.16	1.049E+03	15.61
2005	67	20	18	10.02	1.5	7.15	2.611E+03	>17.00
2005	67	20	18	10.02	2	7.15	3.481E+03	>17.00
2005	67	20	18	10.02	3	7.14	5.200E+03	>17.00
2005	67	20	18	10.02	10	7.15	1.741E+04	14.17
2005	67	21	18	9.59	2	7.15	3.481E+03	9.86
2005	67	21	18	9.59	3	7.14	5.200E+03	9.89
2005	67	21	18	9.59	10	7.15	1.741E+04	16.62
2005	67	21	52	9.30	1.5	7.15	2.611E+03	14.50
2005	67	21	52	9.30	2	7.15	3.481E+03	14.52
2005	67	21	52	9.30	3	7.14	5.200E+03	16.70
2005	67	21	52	9.30	10	7.15	1.741E+04	9.49
2005	67	22	41	8.90	10	7.15	1.741E+04	9.49
2005	67	23	10	8.71	0.1	7.15	1.741E+02	9.74
2005	67	23	10	8.71	0.6	7.16	1.049E+03	9.78
2005	67	23	10	8.71	2	7.15	3.481E+03	9.83
2005	67	23	10	8.71	3	7.14	5.200E+03	9.88
2005	67	23	10	8.71	10	7.15	1.741E+04	16.62
2005	68	0	51	7.87	0.1	7.15	1.741E+02	9.03
2005	68	0	51	7.87	0.6	7.16	1.049E+03	9.09
2005	68	0	51	7.86	1.5	7.15	2.611E+03	9.84
2005	68	0	51	7.85	2	7.15	3.481E+03	9.86
2005	68	0	51	7.85	3	7.14	5.200E+03	9.84
2005	68	0	51	7.79	10	7.15	1.741E+04	8.56
2005	68	2	17	7.18	0.1	7.15	1.741E+02	9.00
2005	68	2	17	7.18	0.6	7.16	1.049E+03	9.09
2005	68	2	17	7.18	1.5	7.15	2.611E+03	9.22
2005	68	2	17	7.15	2	7.15	3.481E+03	9.82
2005	68	2	17	7.13	3	7.14	5.200E+03	9.84
2005	68	2	17	7.13	10	7.15	1.741E+04	8.56
2005	68	3	17	6.58	0.1	7.15	1.741E+02	9.00
2005	68	3	17	6.58	0.6	7.16	1.049E+03	9.21
2005	68	3	17	6.58	1.5	7.15	2.611E+03	9.72
2005	68	3	17	6.66	2	7.15	3.481E+03	9.82
2005	68	3	17	6.64	3	7.14	5.200E+03	8.69
2005	68	3	17	6.62	10	7.15	1.741E+04	8.56
2005	68	19	50	6.55	6	7.03	9.927E+03	7.98
2005	68	19	50	6.55	10	7.03	1.654E+04	8.63
2005	68	20	50	7.03	10	7.03	1.654E+04	>9.40
2005	68	20	50	7.03	20	7.03	3.309E+04	>9.40
2005	68	21	20	7.30	10	7.03	1.654E+04	>9.40
2005	68	21	20	7.30	20	7.03	3.309E+04	>9.40
2005	89	6	50	6.09	0.1	7.33	1.875E+02	7.13
2005	89	6	50	6.09	0.3	7.33	5.626E+02	7.13
2005	89	6	50	6.09	0.6	7.33	1.125E+03	7.13
2005	89	6	50	6.09	1	7.33	1.875E+03	7.13
2005	89	6	50	6.11	3	7.33	5.626E+03	6.73
2005	89	6	50	6.11	6	7.33	1.125E+04	6.59
2005	89	9	25	7.33	3	7.33	5.626E+03	9.16

Table A1
Continued

Year	Day	Hour	Minute	L (event)	$E(L_0)$ (keV)	L_0	μ (keV/G)	L (map)
2005	89	9	25	7.33	6	7.33	1.125E+04	8.67
2005	89	9	25	7.33	10	7.33	1.875E+04	8.61
2005	89	9	25	7.33	20	7.33	3.751E+04	8.01
2005	303	7	40	7.01	3	7	4.900E+03	9.40
2005	303	7	40	7.01	6	7	9.800E+03	9.03
2005	303	7	40	7.01	10	7	1.633E+04	9.13
2005	303	7	40	7.01	20	7	3.267E+04	>9.40
2005	358	9	23	8.42	3	8.24	7.993E+03	13.10
2005	358	9	23	8.42	6	8.24	1.599E+04	13.01
2005	358	9	23	8.42	10	8.24	2.664E+04	11.02
2005	358	9	50	8.23	3	8.24	7.993E+03	13.00
2005	358	9	50	8.23	6	8.24	1.599E+04	13.10
2005	358	9	50	8.23	10	8.24	2.664E+04	11.01
2005	358	16	10	5.62	0.1	5.63	8.498E+01	7.45
2005	358	16	10	5.62	0.3	5.63	2.549E+02	7.51
2005	358	16	10	5.62	0.6	5.63	5.099E+02	7.51
2005	358	16	10	5.62	1	5.63	8.498E+02	7.52
2005	358	16	10	5.62	3	5.63	2.549E+03	7.53
2005	358	16	10	5.62	6	5.63	5.099E+03	7.71
2005	358	16	10	5.62	10	5.63	8.498E+03	7.70
2005	358	16	12	5.51	0.1	5.63	8.498E+01	7.74
2005	358	16	12	5.51	0.3	5.63	2.549E+02	7.73
2005	358	16	12	5.51	0.6	5.63	5.099E+02	7.73
2005	358	16	12	5.51	1	5.63	8.498E+02	7.52
2005	358	16	12	5.51	3	5.63	2.549E+03	7.63
2005	358	16	12	5.51	6	5.63	5.099E+03	7.62
2005	358	16	12	5.51	10	5.63	8.498E+03	6.60
2005	359	2	50	5.72	0.1	5.63	8.498E+01	6.57
2005	359	2	50	5.72	0.3	5.63	2.549E+02	6.74
2005	359	2	50	5.72	0.6	5.63	5.099E+02	6.82
2005	359	2	50	5.72	1	5.63	8.498E+02	6.95
2005	359	2	50	5.72	3	5.63	2.549E+03	6.97
2005	359	2	50	5.72	6	5.63	5.099E+03	7.18
2005	359	8	10	7.90	6	8.24	1.599E+04	>9.40
2005	359	8	10	7.90	10	8.24	2.664E+04	>9.40
2005	359	8	10	7.90	20	8.24	5.328E+04	>9.40
2006	80	4	30	7.27	0.1	7.37	1.906E+02	8.23
2006	80	4	30	7.29	0.3	7.37	5.719E+02	8.24
2006	80	4	30	7.29	0.6	7.37	1.144E+03	8.25
2006	80	4	30	7.29	1	7.37	1.906E+03	8.30
2006	80	4	30	7.29	3	7.37	5.719E+03	8.39
2006	80	4	30	7.29	6	7.37	1.144E+04	8.31
2006	80	4	30	7.29	10	7.37	1.906E+04	8.32
2006	80	4	30	7.29	20	7.37	3.813E+04	8.40
2006	80	4	48	7.38	0.1	7.37	1.906E+02	8.23
2006	80	4	48	7.41	0.3	7.37	5.719E+02	8.29
2006	80	4	48	7.41	0.6	7.37	1.144E+03	8.30
2006	80	4	48	7.41	1	7.37	1.906E+03	8.30
2006	80	4	48	7.41	3	7.37	5.719E+03	8.32
2006	80	4	48	7.41	6	7.37	1.144E+04	8.30
2006	80	4	48	7.41	10	7.37	1.906E+04	8.32
2006	80	4	48	7.41	20	7.37	3.813E+04	8.43
2006	80	5	20	7.57	0.1	7.37	1.906E+02	8.25
2006	80	5	20	7.59	0.3	7.37	5.719E+02	8.27
2006	80	5	20	7.59	0.6	7.37	1.144E+03	8.31
2006	80	5	20	7.59	1	7.37	1.906E+03	8.39
2006	80	5	20	7.59	3	7.37	5.719E+03	8.92
2006	80	5	20	7.59	6	7.37	1.144E+04	8.43
2006	80	5	20	7.59	10	7.37	1.906E+04	8.42
2006	80	5	20	7.59	20	7.37	3.813E+04	8.47

Table A1
Continued

Year	Day	Hour	Minute	L (event)	E(L_0) (keV)	L_0	μ (keV/G)	L (map)
2007	320	23	50	6.54	0.3	6.56	4.033E+02	7.53
2007	320	23	50	6.54	0.6	6.56	8.066E+02	>8.41
2007	320	23	50	6.54	1	6.56	1.344E+03	>8.41
2007	320	23	50	6.54	3	6.56	4.033E+03	>8.41
2007	320	23	50	6.54	6	6.56	8.066E+03	>8.41
2007	320	23	50	6.54	10	6.56	1.344E+04	7.57
2007	321	1	10	5.92	0.3	6.56	4.033E+02	7.11
2007	321	1	10	5.92	0.6	6.56	8.066E+02	7.10
2007	321	1	10	5.92	1	6.56	1.344E+03	7.38
2007	321	1	10	5.92	3	6.56	4.033E+03	7.33
2007	321	1	10	5.92	6	6.56	8.066E+03	7.32
2007	321	1	10	5.92	10	6.56	1.344E+04	7.58
2007	321	2	15	5.40	0.3	6.56	4.033E+02	6.76
2007	321	2	15	5.40	0.6	6.56	8.066E+02	6.78
2007	321	2	15	5.40	1	6.56	1.344E+03	6.86
2007	321	2	15	5.40	3	6.56	4.033E+03	7.34
2007	321	2	15	5.40	6	6.56	8.066E+03	7.55
2007	321	2	15	5.40	10	6.56	1.344E+04	6.77
2010	118	4	0	5.60	0.1	5.59	8.318E+01	7.42
2010	118	4	0	5.60	0.3	5.59	2.495E+02	7.73
2010	118	4	0	5.60	0.6	5.59	4.991E+02	7.73
2010	118	4	0	5.60	1	5.59	8.318E+02	8.78
2010	118	4	0	5.60	3	5.59	2.495E+03	9.01
2010	118	4	0	5.60	6	5.59	4.991E+03	7.55
2010	118	4	0	5.60	10	5.59	8.318E+03	7.54
2010	118	8	10	7.60	3	7.6	6.271E+03	10.35
2010	118	8	10	7.60	6	7.6	1.254E+04	10.70
2010	118	8	10	7.60	10	7.6	2.090E+04	10.92
2010	118	8	10	7.60	20	7.6	4.181E+04	10.93
2010	205	20	15	6.00	0.1	6	1.029E+02	6.39
2010	205	20	15	6.00	0.3	6	3.086E+02	6.51
2010	205	20	15	6.00	0.6	6	6.171E+02	6.54
2010	205	20	15	6.00	1	6	1.029E+03	6.54
2010	205	20	15	6.00	3	6	3.086E+03	6.57
2010	205	20	15	6.00	6	6	6.171E+03	6.28
2010	205	20	15	6.00	10	6	1.029E+04	6.18
2010	206	10	20	6.00	3	6	3.086E+03	>9.40
2010	206	10	20	6.00	6	6	6.171E+03	>9.40
2010	206	10	20	6.00	10	6	1.029E+04	7.91
2010	206	10	20	6.00	20	6	2.057E+04	7.40
2011	10	20	33	4.70	0.01	4.71	4.976E+00	5.62
2011	10	20	33	4.70	0.3	4.71	1.493E+02	6.62
2011	10	20	33	4.70	0.6	4.71	2.985E+02	7.11
2011	10	20	33	4.70	1	4.71	4.976E+02	7.08
2011	10	20	33	4.70	3	4.71	1.493E+03	7.02
2011	10	20	33	4.70	6	4.71	2.985E+03	7.09
2011	10	20	33	4.70	10	4.71	4.976E+03	6.80
2011	10	20	40	4.76	0.01	4.71	4.976E+00	5.78
2011	10	20	40	4.76	0.3	4.71	1.493E+02	6.69
2011	10	20	40	4.76	0.6	4.71	2.985E+02	7.17
2011	10	20	40	4.76	1	4.71	4.976E+02	6.29
2011	10	20	40	4.76	3	4.71	1.493E+03	7.07
2011	10	20	40	4.76	10	4.71	4.976E+03	6.73
2011	10	21	8	4.97	0.01	4.71	4.976E+00	5.53
2011	10	21	8	4.97	0.3	4.71	1.493E+02	6.46
2011	10	21	8	4.97	0.6	4.71	2.985E+02	7.09
2011	10	21	8	4.97	1	4.71	4.976E+02	7.29
2011	10	21	8	4.97	3	4.71	1.493E+03	7.88
2011	10	21	8	4.97	6	4.71	2.985E+03	7.22
2011	10	21	8	4.97	10	4.71	4.976E+03	7.14

Table A1
Continued

Year	Day	Hour	Minute	L (event)	E(L_0) (keV)	L_0	μ (keV/G)	L (map)
2011	10	21	8	4.97	20	4.71	9.951E+03	7.17
2011	10	21	23	5.09	0.01	4.71	4.976E+00	5.82
2011	10	21	23	5.09	0.3	4.71	1.493E+02	7.47
2011	10	21	23	5.09	0.6	4.71	2.985E+02	7.44
2011	10	21	23	5.09	1	4.71	4.976E+02	7.19
2011	10	21	23	5.09	3	4.71	1.493E+03	7.28
2011	10	21	23	5.09	6	4.71	2.985E+03	7.87
2011	10	21	23	5.09	10	4.71	4.976E+03	7.30
2011	10	21	23	5.09	20	4.71	9.951E+03	7.11
2011	11	6	52	9.04	0.3	9.04	1.055E+03	>12.40
2011	11	6	52	9.04	0.6	9.04	2.111E+03	>12.40
2011	11	6	52	9.04	1	9.04	3.518E+03	>12.40
2011	11	6	52	9.04	3	9.04	1.055E+04	>12.40
2011	11	6	52	9.04	6	9.04	2.111E+04	9.56
2011	11	6	52	9.15	10	9.04	3.518E+04	9.57
2011	11	6	52	9.15	20	9.04	7.036E+04	9.80
2011	107	1	55	6.72	0.1	5.16	6.542E+01	7.15
2011	107	1	55	6.72	0.3	5.16	1.963E+02	7.22
2011	107	1	55	6.72	0.6	5.16	3.925E+02	7.26
2011	107	1	55	6.72	1	5.16	6.542E+02	7.55
2011	107	1	55	6.72	3	5.16	1.963E+03	6.92
2011	107	1	55	6.72	6	5.16	3.925E+03	6.81
2011	107	1	55	6.72	10	5.16	6.542E+03	6.87
2011	107	2	4	6.53	0.1	5.16	6.542E+01	6.86
2011	107	2	4	6.53	0.3	5.16	1.963E+02	6.86
2011	107	2	4	6.53	0.6	5.16	3.925E+02	6.83
2011	107	2	4	6.53	1	5.16	6.542E+02	6.83
2011	107	2	4	6.53	3	5.16	1.963E+03	6.83
2011	107	2	4	6.53	6	5.16	3.925E+03	6.84
2011	107	2	4	6.53	10	5.16	6.542E+03	6.79
2011	107	5	50	5.32	0.1	5.16	6.542E+01	6.92
2011	107	5	50	5.32	0.3	5.16	1.963E+02	6.86
2011	107	5	50	5.32	0.6	5.16	3.925E+02	6.83
2011	107	5	50	5.32	1	5.16	6.542E+02	6.83
2011	107	5	50	5.32	3	5.16	1.963E+03	6.90
2011	107	5	50	5.32	6	5.16	3.925E+03	6.84
2011	107	5	50	5.32	10	5.16	6.542E+03	6.83
2011	107	5	50	5.32	20	5.16	1.308E+04	6.81
2011	107	6	10	5.17	0.1	5.16	6.542E+01	6.93
2011	107	6	10	5.17	0.3	5.16	1.963E+02	6.90
2011	107	6	10	5.17	0.6	5.16	3.925E+02	6.89
2011	107	6	10	5.17	1	5.16	6.542E+02	6.84
2011	107	6	10	5.17	3	5.16	1.963E+03	6.90
2011	107	6	10	5.17	6	5.16	3.925E+03	6.89
2011	107	6	10	5.17	10	5.16	6.542E+03	6.88
2011	107	6	10	5.17	20	5.16	1.308E+04	6.82
2011	107	7	29	4.93	0.1	5.16	6.542E+01	6.91
2011	107	7	29	4.93	0.3	5.16	1.963E+02	6.83
2011	107	7	29	4.93	0.6	5.16	3.925E+02	6.83
2011	107	7	29	4.93	1	5.16	6.542E+02	6.83
2011	107	7	29	4.93	3	5.16	1.963E+03	6.81
2011	107	7	29	4.93	6	5.16	3.925E+03	6.79
2011	107	7	29	4.93	10	5.16	6.542E+03	6.79
2011	107	7	29	4.93	20	5.16	1.308E+04	6.81

a function of the L value of the observed injection. The diagonal lines labeled "0," "1," "2," and "3" show the locations where displacements of 0, 1, 2, or 3 R_S from origin to observation would occur. The three events analyzed by Paranicas et al. (2016) are shown as red dots in Figure A2, and the events analyzed by Rymer et al. (2009) are shown as blue dots.

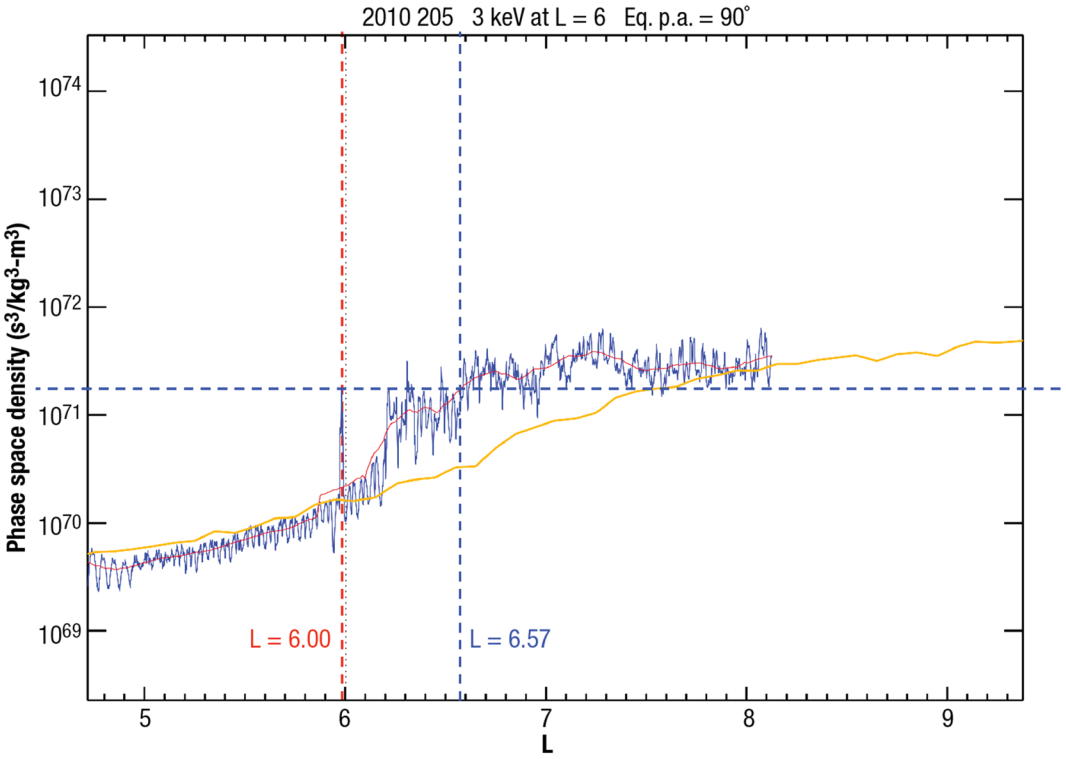

Figure A1. Sample PSD mapping from an injection at L = 6 to a proposed starting location at L = 6.57 based on the intersection of the horizontal straight blue line with the red line. The red line is a smoothing of the jagged blue line representing the recent PSD measurements (see Appendix). The gold line is a mission average for comparison.

Figure A2 shows that beyond L ~ 8, the PSD mapping procedure produces rather uncertain results, but inside L ~ 8, the multiple μ profiles for each injection produce fairly consistent values of the mapped origin. It appears from this plot that at the lower range of L (<8), the origin of the injections is typically less than about 3 R_S from the point of observation, with a number of events having propagated only a fraction of one R_S. In the full set of injections/μ values, 94% have travel distances less than 3.5 R_S, and the median value is 1.6 R_S. The figure also shows that aside from the injections observed beyond L ~ 8, only one of the observed events appears to have traveled from L ~ 10 or larger.

The results shown in Figure A2 are puzzling in the context of a paradigm in which injection channels are created in a particularly unstable range of L, propagating inward from there. Thomsen and Coates (2019) have argued that the radial distance at which Saturn's magnetospheric electron population transitions from mostly dense with some tenuous intervals (inner magnetosphere) to mostly tenuous with some dense intervals (outer magnetosphere) can plausibly be attributed to the boundary between flux tubes that have undergone nightside reconnection and those that have not (see also Thomsen et al., 2015). The sharp radial gradient that would result from such reconnection would presumably be unstable to the interchange instability (e.g., Southwood & Kivelson, 1987), spawning inward propagating injections and outward propagating dense plasma. This boundary region, identified by Thomsen and Coates as the "plasmapause," was found to be near L ~ 10. Hence, under this scenario, one might expect that interchange injections would originate at or near the plasmapause at L ~ 10.

In contrast to this expectation, the results shown in Figure A2 suggest a picture in which injections randomly arise at various points on a background density gradient and travel only a relatively short distance. Such a "bubbling" scenario would produce a much more diffusive transport for the entry of energetic particles than the deeply penetrating channels heretofore envisioned.

Alternatively, it could be that precipitation losses during injection transport are in fact quite substantial, so our assumption of conserved PSD for the matching is not correct. Rymer et al. (2007) have calculated the

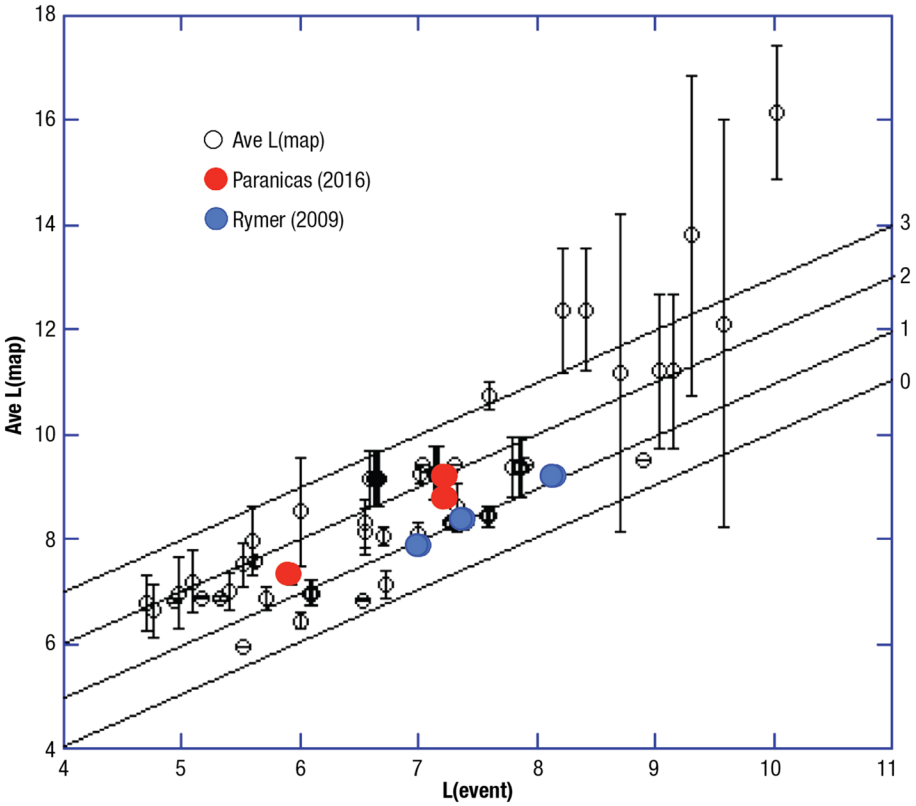

Figure A2. Mapping of all events to starting locations with four diagonal lines showing the range in L of the injection distance from start to end (see the Appendix for a complete discussion). Some reference examples are added. The figure illustrates the small delta L involved in events of this type, based on our analysis.

time to lose 80% of an electron population due to strong pitch angle scattering. Their Figure 8c shows that for electrons in the range of 1–10 keV, this loss time is greater than several hours at L ~ 5, and by L ~ 7, it is greater than 20 hours. For the 20 events examined in this paper, all have estimated travel times well below this loss time for 1 keV electrons, and all but one even have travel times well below the loss time for 10 keV. Thus, it appears unlikely that very significant precipitation losses could occur during the injection travel time. Another avenue for future exploration is the loss of electron energy in the neutral medium. Paranicas, Mitchell, Roussos, et al. (2010) discussed the pitch angle scattering and energy loss of tens of keV electrons moving through a neutral population and cited experimental work on the subject. In a falling energy spectrum, gradual energy loss means that the measured j at a specific energy will decrease over time, everything else being the same.

While it is not within the scope of the present study, it would be valuable to examine where the inferred start locations of these injections are positioned relative to the general gradient in the flux tube content for each of these passes. Such a study would help distinguish between "bubbling" from random spots on the gradient and a more coherent onset at the edge of the inner region.

Data Availability Statement

All the Cassini CAPS data are available through NASA's Planetary Data System (PDS) and can be found at https://pds-ppi.igpp.ucla.edu/, by choosing Saturn and then CAPS.

Acknowledgments

We thank N. Sergis and C. Jackman, who with the first author, coled an ISSI team whose members initiated a lot of our work on Saturn injections. This research project was supported by a grant between the Johns Hopkins University and NASA (NNX16AI46G).

References

Andre, N., Dougherty, M. K., Russell, C. T., Leisner, J. S., & Khurana, K. K. (2005). Dynamics of the Saturnian inner magnetosphere: First inferences from the Cassini magnetometers about small-scale plasma transport in the magnetosphere. *Geophysical Research Letters*, *32*, L14S06. https://doi.org/10.1029/2005GL022643

Andre, N., Persoon, A. M., Goldstein, J., Burch, J. L., Louarn, P., Lewis, G. R., et al. (2007). Magnetic signatures of plasma-depleted flux tubes in the Saturnian inner magnetosphere. *Geophysical Research Letters*, *34*, L14108. https://doi.org/10.1029/2007GL030374

Azari, A. R., Liemohn, M. W., Jia, X., Thomsen, M. F., Mitchell, D. G., Sergis, N., et al. (2018). Interchange injections at Saturn: Statistical survey of energetic H+ sudden flux intensifications. *Journal of Geophysical Research: Space Physics*, *123*, 4692–4711. https://doi.org/10.1029/2018JA025391

Burch, J. L., Goldstein, J., Hill, T. W., Young, D. T., Crary, F. J., Coates, A. J., et al. (2005). Properties of local plasma injections in Saturn's magnetosphere. *Geophysical Research Letters*, *32*, L14SO2. https://doi.org/10.1029/2005GL022611

Chen, Y., Hill, T. W., Rymer, A. M., & Wilson, R. J. (2010). Rate of radial transport of plasma in Saturn's inner magnetosphere. *Journal of Geophysical Research*, *115*, A10211. https://doi.org/10.1029/2010JA015412

Hill, T. W., Rymer, A. M., Burch, J. L., Crary, F. J., Young, D. T., Thomsen, M. F., et al. (2005). Evidence for rotationally driven plasma transport in Saturn's magnetosphere. *Geophysical Research Letters*, *32*, L14S10. https://doi.org/10.1029/2005GL022620

Liu, X., Hill, T. W., Wolf, R. A., Sazykin, S., Spiro, R. W., & Wu, H. (2010). Numerical simulation of plasma transport in Saturn's inner magnetosphere using the Rice Convection Model. *Journal of Geophysical Research*, *115*, A12254. https://doi.org/10.1029/2010JA015859

Mauk, B. H., Saur, J., Mitchell, D. G., Roelof, E. C., Brandt, P. C., Armstrong, T. P., et al. (2005). Energetic particle injections in Saturn's magnetosphere. *Geophysical Research Letters*, *32*, L14S05. https://doi.org/10.1029/2005GL022485

Paranicas, C., Mitchell, D. G., Krimigis, S. M., Carbary, J. F., Brandt, P. C., Turner, F. S., et al. (2010). Asymmetries in Saturn's radiation belts. *Journal of Geophysical Research*, *115*, A07216. https://doi.org/10.1029/2009JA014971

Paranicas, C., Mitchell, D. G., Roussos, E., Kollmann, P., Krupp, N., Müller, A. L., et al. (2010). Transport of energetic electrons into Saturn's inner magnetosphere. *Journal of Geophysical Research*, *115*, A09214. https://doi.org/10.1029/2010JA015853

Paranicas, C., Thomsen, M. F., Achilleos, N., Andriopoulou, M., Badman, S. V., Hospodarsky, G., et al. (2016). Effects of radial motion on interchange injections at Saturn. *Icarus*, *264*, 342–351. https://doi.org/10.1016/j.icarus.2015.10.002

Rymer, A., Mauk, B. H., Hill, T. W., André, N., Mitchell, D. G., Paranicas, C., et al. (2009). Cassini evidence for rapid interchange transport at Saturn. *Planetary and Space Science*, *57*(14-15), 1779–1784. https://doi.org/10.1016/j.pss.2009.04.010

Rymer, A., Mauk, B. H., Hill, T. W., Paranicas, C., André, N., Sittler, E. C. Jr., et al. (2007). Electron sources in Saturn's magnetosphere. *Journal of Geophysical Research*, *112*, A02201. https://doi.org/10.1029/2006JA012017

Schulz, M. (1998). Particle drift and loss rates under strong pitch angle diffusion in Dungey's model magnetosphere. *Journal of Geophysical Research: Space Physics*, *103*(A1), 61–67. https://doi.org/10.1029/97ja02042

Southwood, D. J., & Kivelson, M. G. (1987). Magnetospheric interchange instability. *Journal of Geophysical Research*, *92*, 109.

Thomsen, M., & van Allen, J. A. (1980). Motion of trapped electrons and protons in Saturn's inner magnetosphere. *Journal of Geophysical Research*, *85*, 5831–5834.

Thomsen, M. F. (2013). Saturn's magnetospheric dynamics. *Geophysical Research Letters*, *40*, 5337–5344. https://doi.org/10.1002/2013GL057967

Thomsen, M. F., & Coates, A. J. (2019). Saturn's plasmapause: Signature of magnetospheric dynamics. *Journal of Geophysical Research: Space Physics*, *124*, 8804–8813. https://doi.org/10.1029/2019JA027075

Thomsen, M. F., Mitchell, D. G., Jia, X., Jackman, C. M., Hospodarsky, G., & Coates, A. J. (2015). Plasmapause formation at Saturn. *Journal of Geophysical Research: Space Physics*, *120*, 2571–2583. https://doi.org/10.1002/2015JA021008

Walt, M. (1994). *Introduction to geomagnetically trapped radiation*. Cambridge: Cambridge University Press. https://doi.org/10.1017/CBO9780511524981

Wilson, R. J., Bagenal, F., & Persoon, A. M. (2017). Survey of thermal plasma ions in Saturn's magnetosphere utilizing a forward model. *Journal of Geophysical Research: Space Physics*, *122*, 7256–7278. https://doi.org/10.1002/2017JA024117

Wilson, R. J., Tokar, R. L., Henderson, M. G., Hill, T. W., Thomsen, M. F., & Pontius, D. H. Jr. (2008). Cassini plasma spectrometer thermal ion measurements in Saturn's inner magnetosphere. *Journal of Geophysical Research*, *113*, A12218. https://doi.org/10.1029/2008JA013486

Young, D. T., Berthelier, J. J., Blanc, M., Burch, J. L., Coates, A. J., Goldstein, R., et al. (2004). Cassini plasma spectrometer investigation. *Space Science Reviews*, *114*(1-4), 1–112. https://doi.org/10.1007/s11214-004-1406-4